

# Efficient and Comprehensive Feature Extraction in Large Vision-Language Model for Clinical Pathology Analysis

Shengxuming Zhang<sup>1</sup>, Weihai Li<sup>1</sup>, Tianhong Gao<sup>1</sup>, Jiacong Hu<sup>2</sup>,  
Haoming Luo<sup>1</sup>, Mingli Song<sup>2</sup>, Xiuming Zhang<sup>3</sup>, Zunlei Feng<sup>1,2\*</sup>

<sup>1</sup>School of Software Technology, Zhejiang University

<sup>2</sup>College of Computer Science and Technology, Zhejiang University

<sup>3</sup>First Affiliated Hospital, College of Medicine, Zhejiang University

## Abstract

*Pathological diagnosis is vital for determining disease characteristics, guiding treatment, and assessing prognosis, relying heavily on detailed, multi-scale analysis of high-resolution whole slide images (WSI). However, traditional pure vision models face challenges of redundant feature extraction, whereas existing large vision-language models (LVLMs) are limited by input resolution constraints, hindering their efficiency and accuracy. To overcome these issues, we propose two innovative strategies: the mixed task-guided feature enhancement, which directs feature extraction toward lesion-related details across scales, and the prompt-guided detail feature completion, which integrates coarse- and fine-grained features from WSI based on specific prompts without compromising inference speed. Leveraging a comprehensive dataset of 490,000 samples from diverse pathology tasks—including cancer detection, grading, vascular and neural invasion identification, and so on—we trained the pathology-specialized LVLM, Omni-Path. Extensive experiments demonstrate that this model significantly outperforms existing methods in diagnostic accuracy and efficiency, offering an interactive, clinically aligned approach for auxiliary diagnosis in a wide range of pathology applications.*

## 1. Introduction

Pathological diagnosis, as the “gold standard” of disease diagnosis, holds an irreplaceable central position in clinical diagnostics. Through microscopic morphological examination of patient tissues and cells, it not only determines the nature, type, and staging of diseases but also provides critical information for clinical treatment planning, prognosis assessment, and efficacy monitoring. The emergence and development of digital pathology are transforming this

traditional field. By using high-resolution scanning equipment to convert glass slides into whole slide images (WSI), digital pathology overcomes the limitations of conventional pathology that rely on microscopy, enabling remote consultations and real-time consultations while paving new paths for medical education, research collaborations, and long-term clinical data storage.

WSI is characterized by ultra-high resolution, with single images typically exceeding  $50,000 \times 50,000$  pixels. This high resolution allows WSI to encompass a wealth of multi-scale features, from organ-level structures to cellular-level details. However, only a subset of these features is directly relevant to disease diagnosis. Pathologists must therefore observe the slides at multiple magnifications to comprehensively capture morphological characteristics of lesions at various scales, identifying the key features closely related to diagnosis to avoid misdiagnosis or missed diagnoses.

In the field of digital pathology, artificial intelligence is playing an increasingly vital role [15, 16, 52, 54]. Many pure vision deep learning models have been developed to assist in the diagnosis of pathology WSIs [10, 11, 45, 46, 51]. With the rapid development of large language models (LLM) [1, 5, 14, 34, 43, 44] and large vision-language models (LVLM) [4, 8, 12, 26, 30], these models have shown substantial auxiliary capabilities across various domains, and recent research [2, 13, 31, 36, 37, 39–41] has attempted to apply LVLM to pathology. However, existing methods still face significant limitations: traditional pure vision models [10, 11, 45, 46, 51] require WSIs to be divided into thousands of patches, with an encoder network extracting features from each patch and an aggregator network synthesizing the final result. These methods inevitably extract numerous redundant features, leading to a prolonged diagnostic process. Current pathological LVLMs [2, 13, 31, 36, 37, 39–41, 49], due to input constraints, can only process either single pathological image patches or low-resolution thumbnails of WSI. While this

\*Corresponding author, email: zunleifeng@zju.edu.cn

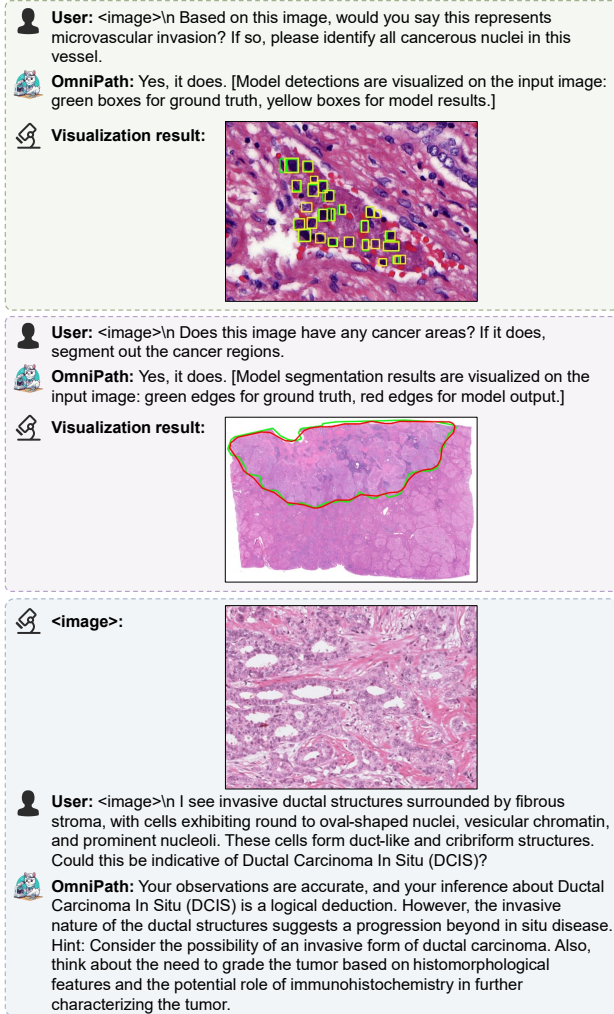


Figure 1. From top to bottom are examples of our OmniPath, a vision-language model optimized for pathology, applied to referring expression detection, segmentation, and visual question answering. Notably, in the first example, OmniPath is tasked with detecting cancer cell nuclei within blood vessels. Results show that OmniPath accurately identifies most nuclei within vessels without mistakenly detecting any outside, demonstrating its capability to understand pathological concepts and reason effectively.

improves processing speed, it either lacks global information for single patches or loses substantial detail information for WSI, making it difficult to meet clinical assisted diagnostic requirements. Furthermore, experimental analysis (given in Section 3) of image tokens that LVLMM focuses on for decision-making reveals that existing LVLMMs often overly emphasize the features of a few key tokens in the input image. While this feature extraction pattern can summarize image content, it fails to comprehensively capture multi-scale features related to lesions, thus affecting the model’s diagnostic performance.

To enhance the accuracy and reliability of intelligent pathological diagnosis and analysis, we have developed an efficient and comprehensive feature extraction scheme specifically tailored for LVLMM in pathology, providing complete, multi-scale feature support for various types of pathological diagnostic analysis tasks. To address the issue of the model focusing only on a few key tokens of the image, we introduce the mixed task-guided feature enhancement (MTGFE) strategy. Through adding instruction-following data for detecting and segmenting diverse pathological concepts, coupled with corresponding model module improvements, we enhance the model’s ability to perceive lesion-related detailed features across the whole image while achieving full coverage of visual task types in pathological analysis. Furthermore, given the need for multi-scale features in pathology slide analysis, we designed the prompt-guided detail feature completion (PGDFC) strategy. This strategy first captures the coarse-grained global features of a WSI and then, based on specific task requirements provided by prompts, extracts fine-grained features from key focus areas. By merging coarse- and fine-grained features, this approach enhances accuracy across tasks while avoiding the input of exhaustive detail features, thereby maintaining high inference speed.

To make LVLMM truly applicable to clinical pathology for auxiliary diagnosis, we gathered visual instruction-following data for multiple organs and tasks from several institutions, based on diagnostic items in actual pathology reports. This data trains the model to meet the diverse clinical needs of pathologists through human-computer interaction. These tasks include cancer region detection and segmentation, cancer grading and classification, identification of vascular and neural invasion, and lymph node metastasis detection, among others, with each task containing meticulously compiled datasets ranging from hundreds to thousands of instruction-following data samples. Furthermore, to strengthen the model’s understanding of foundational pathology concepts, we collected training data for fundamental tasks such as nucleus detection and classification, vascular and neural detection, lymph node detection, and tumor-infiltrating lymphocyte identification. Additionally, we integrated pathology image-text data from publicly available online resources, including the PubMed database [17, 40], pathology textbooks and atlases [20, 40], The Cancer Genome Atlas (TCGA) [9, 39], Twitter posts [21, 41], and educational histopathology videos on YouTube [22, 36]. This integration yielded a comprehensive dataset covering 20 organs with approximately 490,000 training samples. Leveraging our efficient and comprehensive feature extraction scheme and this extensive dataset, we trained OmniPath, a specialized LVLMM for pathology, capable of providing comprehensive pathology auxiliary diagnostic services through human-computer interaction.

Extensive experimental results demonstrate that OmniPath outperforms existing pathology LVLMs across a range of diagnostic tasks, better aligning with the actual needs of clinical practice.

In conclusion, the main contributions of our work are summarized as follows:

- We propose the mixed task-guided feature enhancement strategy, which guides large vision-language model to capture detailed features in pathology images by constructing fine-grained tasks focused on local image features and integrating corresponding improvements in model architecture. This effectively addresses the model’s tendency to rely excessively on global features represented by a few key tokens of the image.
- The prompt-guided detail feature completion strategy is devised to supplement key region detail features based on specific task requirements, significantly improving the accuracy of various pathology slide analysis tasks while maintaining high inference efficiency.
- We integrated multi-source data to construct a pathology visual instruction tuning dataset covering 20 organs with approximately 490,000 training samples. Based on this dataset, we trained the OmniPath pathology large vision-language model. Extensive experimental validation shows that OmniPath surpasses existing pathology large vision-language models across various diagnostic tasks, aligning more closely with clinical pathology diagnostic needs through an interactive paradigm.

## 2. Related Work

**Pure vision deep models** have been applied to pathology image analysis for quite some time. Early research primarily focused on designing specialized model architectures for specific tasks, including nuclei segmentation [15], vessel segmentation [16], microvascular invasion detection [54], and cancer grading [52]. In contrast, research on overall pathology WSI analysis tasks, such as cancer subtyping, metastasis detection, and prognosis prediction, commonly adopts a multiple instance learning (MIL) approach [23, 38, 42, 50]. This approach treats an entire WSI as a “bag”, partitioning the WSI into tens of thousands of patches similar in size to conventional images, with each patch considered an “instance.” In practice, researchers typically employ an encoder network to extract features from each patch and then aggregate these features to produce an analysis result for the entire WSI.

To enhance the transferability and generalization of these methods, recent efforts have focused on self-supervised training of the patch encoder using vast amounts of unlabeled WSIs [10, 11, 45, 46, 51]. These self-supervised approaches significantly improve performance across various general tasks and bolster the model’s ability to identify rare diseases. However, this approach often requires substan-

tial time to extract features from each patch, and critical disease-related features may be obscured by an overwhelming number of unrelated features.

**Large vision-language models** have also been explored for pathology image analysis in the past year [2, 13, 31, 36, 37, 39–41, 49]. These models typically utilize LLaVA-based architectures [30], fine-tuned with instruction-following data curated through various methods and sources. PathAsst [40] gathered image-caption pairs from the PubMed database and internal materials to train a CLIP [35] model, replacing LLaVA’s vision encoder, and leveraged ChatGPT [34] to transform simple image-caption data into more complex instruction-following data, which also included instructions for invoking specialized models as needed. Quilt-LLaVA [36] utilized the mouse pointer trails from speakers in YouTube tutorial videos to pinpoint the pathology concept being explained, then constructed instruction-following data using GPT-4 [1]. PathMMU [41] integrated data from multiple sources to build a pathology visual question-answering training and evaluation dataset, with seven pathology experts reviewing the test set to ensure authoritative evaluation. PathAlign [2] employed a Q-Former structure from BLIP-2 [28] to extract features from WSIs as inputs for the LLM, while PA-LLaVA [13] developed a scale-invariant connector to prevent information loss from image resizing.

However, due to structural limitations, most of these models can only accept standard-sized images, handling only single pathology image patches or low-resolution WSI thumbnails. As a result, they lack global context for single patches and lose significant detail for WSIs, posing challenges for clinical diagnostic support. Although PathAlign [2] enables full WSI input, it still requires feature extraction from each patch. Furthermore, these models are typically limited to image description tasks or visual question-answering for image classification, lacking the capability for fine-grained tasks like detection and segmentation, as well as complex reasoning tasks that require multiple diagnostic steps.

## 3. Analysis of Drawback in Existing LVLM

### 3.1. Preliminaries

Today’s most prominent open-source LVLM, like LLaVA [30], successfully integrate vision and language capabilities. For input pair  $x = (x_v, x_t)$ , where  $x_v$  represents the image and  $x_t$  represents the text prompt, the model first processes them through two embedding networks: vision encoder  $\mathcal{V}$ , consisting of a CLIP-based Vision Transformer (ViT) [35] followed by a projection layer, maps the image into feature embedding  $e_v = (e_v^1, \dots, e_v^N)$  where  $N$  is the number of image tiles, while text encoder  $\mathcal{T}$ , comprising



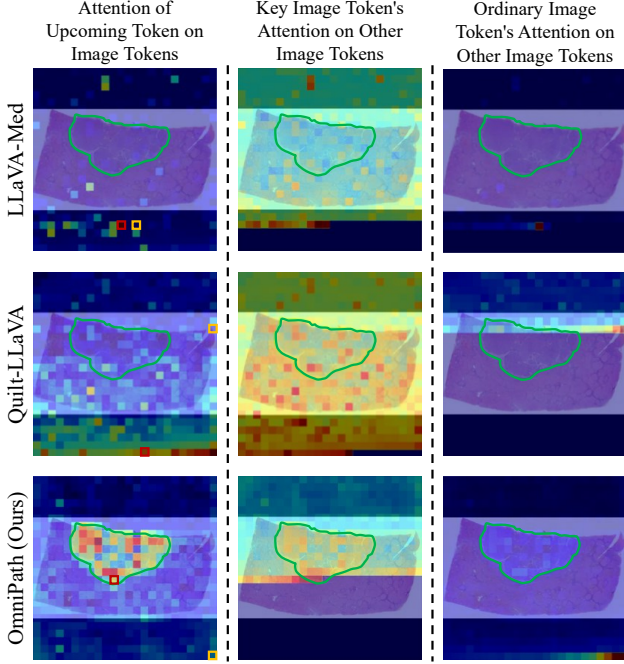


Figure 2. The green contours on the pathology slides mark cancerous regions annotated by pathologists. The first column shows the attention distribution heatmap of the LLM’s final input token over all image tokens, where the intensity of attention values is mapped from blue (low) to red (high). In each row showing different model results, a red box and a yellow box are used to select a key token (with relatively high attention) and an ordinary token (with relatively low attention) respectively. The attention distributions of the selected key token and ordinary token over other image tokens are then visualized in the second and third columns respectively. All experiments were conducted using identical prompts, with attention values extracted from the first layer of the LLM.

a tokenizer and an embedding layer, transforms the text into feature embedding  $e_t = (e_t^1, \dots, e_t^M)$  where  $M$  is the number of text tokens. Both embeddings lie in the same feature space and serve as input to the large language model  $\mathcal{M}$ , which generates the output sequence  $y$ . The model can be formalized as:  $y = \mathcal{M}(e_v, e_t)$ , where  $e_v = \mathcal{V}(x_v)$  and  $e_t = \mathcal{T}(x_t)$ .

### 3.2. Decision-Dependent Image Tokens Analysis

To further investigate the image feature patterns that LVLM relies on during the answer generation and decision-making processes, and to optimize the model to focus more effectively on task-relevant features, thereby improving accuracy in responding to human queries, we conducted an attention pattern analysis on existing medical LVLMs. Specifically, we selected two representative models, LLaVA-Med [27] and Quilt-LLaVA [36], using a unified prompt, “*What cancer subtype is shown in this image?*” to guide the models in performing cancer subtype identification on pathology

slides. Our proposed OmniPath model was included as a comparison. Visualization of the relevant analysis results is shown in Figure 2.

We extracted the attention matrix from the input layer of  $\mathcal{M}$  and averaged the attention values across all heads to obtain matrix  $\Psi \in \mathbb{R}^{(N+M) \times (N+M)}$ . In this matrix, the  $i$ -th row of  $\Psi$  represents the attention distribution of the  $i$ -th embedding token in the input of  $\mathcal{M}$  towards other tokens. Since a decoder-only Transformer model is used,  $\Psi$  takes the form of a lower triangular matrix. To analyze the relationship between the upcoming generated content and the image tokens, we selected the attention values of the final embedding token towards all image tokens, denoted as  $\Psi_{(N+M), e_v} \in \mathbb{R}^N$ , and restored it to a two-dimensional representation of the original image. We then generated a heatmap and overlaid it on the input image for visualization, as shown in the first column of Figure 2.

In the heatmap, attention intensity is mapped from blue (low) to red (high). Cancerous regions in the input pathology slide  $x_v$  are annotated by pathologists with green contours. Ideally, to achieve accurate cancer subtype identification, the model should focus on image features within the cancerous region rather than on other tissue and background areas. However, the heatmaps for LLaVA-Med [27] and Quilt-LLaVA [36] reveal that only a few key image tokens receive high attention weights, and these key tokens are primarily located outside the cancerous regions.

To further analyze the information encoded by these key image tokens, we selected one key image token  $e_v^k$  and one ordinary token  $e_v^o$  from each experiment, and visualized their attention distributions over all image tokens, denoted as  $\Psi_{e_v^k, e_v} \in \mathbb{R}^N$  and  $\Psi_{e_v^o, e_v} \in \mathbb{R}^N$ , respectively. The selected key and ordinary tokens are indicated in the first column of Figure 2 with red and yellow boxes, respectively. The corresponding attention heatmap visualizations are presented in the second and third columns of Figure 2.

Through visual analysis, it can be observed that the key image token  $e_v^k$  exhibits high attention values across all preceding image tokens, whereas the ordinary token  $e_v^o$  focuses only on nearby preceding tokens. This indicates that the primary function of the key token is to aggregate and distill the global semantic information of the entire image for use by the LLM  $\mathcal{M}$ . However, this mechanism has limitations:  $\mathcal{M}$  can only obtain a coarse-grained conceptual representation of the image, which may not only include redundant background information but, more critically, miss essential local lesion features and spatial structure information. This directly results in suboptimal performance of existing pathology LVLMs on diagnostic analysis tasks for pathology WSIs.

In contrast, in the optimized OmniPath model, the heatmap of  $\Psi_{(N+M), e_v}$  shows that key image tokens are concentrated in the cancerous regions, indicating that these

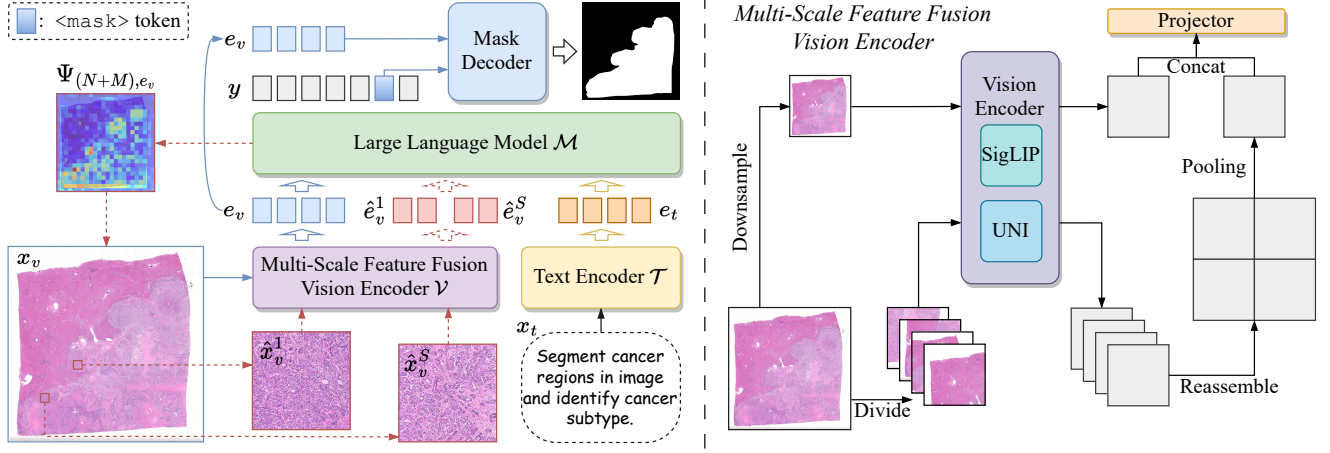


Figure 3. Overview of the proposed OmniPath. Left: the architecture of OmniPath with feature enhancement and completion strategy. Right: the detailed structure of the multi-scale feature fusion vision encoder.

areas contribute more information to  $\mathcal{M}$ , aiding in accurate cancer subtype identification. From the heatmap of  $\Psi_{e_v^k, e_v}$ , it can be seen that although the key token maintains high attention values across all preceding image tokens, its focus on tokens within the cancerous regions is significantly higher. This demonstrates that OmniPath can more precisely capture critical diagnostic features in pathology WSIs, thus achieving a better response to user instructions. The next section will elaborate on the optimization strategies employed in OmniPath.

## 4. Method

To address the identified limitations of existing LVLMs, specifically their tendency to over-rely on key tokens and inability to comprehensively capture multi-scale pathological features, we propose a novel framework that enhances both feature extraction precision and efficiency. Our approach consists of two complementary strategies: the mixed task-guided feature enhancement (MTGFE) and the prompt-guided detail feature completion (PGDFC). These strategies work in concert to improve the model’s capability in pathological image analysis by targeting the core challenges revealed in our previous analysis while maintaining computational efficiency and diagnostic accuracy. OmniPath trained with these two strategies is shown in Figure 3. Below, we elaborate on these strategies and their implementation.

### 4.1. Mixed Task-Guided Feature Enhancement

Currently, pathology LVLMs [13, 31, 36, 40] commonly use the vision encoder from Contrastive Language-Image Pre-Training (CLIP) [35] to convert images into embedding tokens. Although this vision encoder enables alignment between image features and the text space, facilitating the LLM’s understanding of image content, it primarily re-

lies on pre-training data consisting of image-caption pairs. This leads the vision encoder to excel at extracting global features of images but limits its ability to perceive local details and spatial structures. However, in pathological diagnosis, accurately identifying foundational pathological concepts and their spatial relationships within pathology WSIs is essential. For instance, in diagnosing microvascular invasion [54], a pathologist needs to first locate the cancerous region and then inspect surrounding vessels for the presence of cancer cell nuclei, requiring the model to have a nuanced understanding of pathological concepts such as cancerous tissue, blood vessels, normal cell nuclei, and cancer cell nuclei, along with their spatial relationships. Current pathology LVLMs still exhibit limitations in this regard. To address this issue, we focus on both training data and model architecture to enhance the model’s capability in extracting and understanding detailed features.

In terms of training data, we designed a hierarchical instruction fine-tuning dataset covering diverse tasks such as referring expression detection and segmentation, to enhance the pathological feature extraction ability of the visual encoder  $\mathcal{V}$  and the visual feature comprehension ability of the LLM  $\mathcal{M}$ . This dataset systematically constructs concept recognition tasks at three levels: tissue, structure, and cellular, from macro to micro perspectives.

At the tissue level, tasks include detecting and segmenting cancerous regions in WSI thumbnails, as well as detecting lymph nodes. At the structural level, the focus is on detecting and segmenting blood vessels, bile ducts, and nerves, along with recognizing microvascular invasion, neural invasion, and lymph node invasion. At the cellular level, in addition to basic nucleus classification and detection, more complex tasks requiring inferential abilities were designed, such as “detecting cancer cell nuclei within vessels.”

Method	HCC-S	HCC-G	ICC-S	ICC-G	RCC-S	LUNG-S	LUNG-G	STAD-L	STAD-G	MVI	NI	PanCancer	OC	TC	TIL	MSI	GLR-7
LLaVA-1.5	25.76	0.16	16.37	3.97	23.82	21.03	14.66	15.43	9.32	18.15	55.07	3.17	3.81	9.89	51.92	50.02	13.93
LLaVA-Med	31.23	7.78	38.56	16.45	52.34	38.77	36.45	28.12	25.23	16.89	54.67	28.34	21.29	33.88	58.42	47.21	39.87
Quilt-LLaVA	78.34	42.23	68.45	81.56	75.23	83.12	57.89	62.89	61.23	50.78	79.45	44.56	49.67	70.56	77.34	63.12	59.45
PA-LLaVA	82.45	40.56	66.78	79.34	73.67	76.78	60.23	64.89	59.89	61.56	67.12	46.78	48.23	68.45	76.34	62.45	58.67
OmniPath	<b>97.09</b>	<b>63.07</b>	<b>86.04</b>	<b>96.53</b>	<b>90.17</b>	<b>96.55</b>	<b>71.98</b>	<b>91.56</b>	<b>87.59</b>	<b>97.79</b>	<b>93.83</b>	<b>54.44</b>	<b>69.52</b>	<b>86.66</b>	<b>89.88</b>	<b>73.78</b>	<b>79.01</b>

Table 1. Performance comparison on patch-level pathology diagnostic tasks.

To further improve the model’s ability to recognize multidimensional pathological features, we also constructed a cross-scale instruction task set that includes organ recognition, cancer subtype identification and grading, tissue type recognition, microsatellite instability detection, and tumor-infiltrating lymphocyte recognition. These self-constructed datasets, combined with publicly available pathology visual question-answering datasets, have formed a training dataset containing 20 types of organs and approximately 490,000 training samples, significantly enhancing the model’s ability to extract pathological features at multiple scales and granularities. For details on dataset sources and construction methods, please refer to the supplementary material.

In terms of model architecture, we implemented three primary improvements (as shown in Figure 3). First, we added an extra ViT named UNI [11]. This ViT, pretrained on large-scale pathology images using the DINOv2 [33] framework, provides critical fine-grained pathological visual features for detection and segmentation tasks. Second, we adopted a multi-scale feature fusion strategy, enabling the model to handle higher-resolution input images without retraining the vision encoder. Specifically, we set a series of increasing input resolutions based on the original resolution supported by the vision encoder, with other resolutions as integer multiples of this base. For the original resolution images, features are directly extracted via the vision encoder. For higher-resolution images, they are divided into image tiles of the original size, each processed separately for feature extraction, and then reassembled based on spatial position. Finally, the features are averaged to match the original feature map dimensions and concatenated along the channel dimension. This approach allows for richer detail extraction without increasing the number of input image tokens  $e_v$  to the LLM  $\mathcal{M}$ .

Third, we introduced a mask encoder and decoder module and added a new `<mask>` token to the LLM vocabulary to represent segmentation results. The mask encoder encodes binary segmentation maps into embeddings to replace the corresponding `<mask>` positions in the input, while the mask decoder generates segmentation results based on the image embeddings  $e_v$  and the output embedding corresponding to `<mask>`. The segmentation is optimized using per-pixel binary cross-entropy (BCE) loss and DICE loss. Notably, we attempted to add a dedicated bounding box encoder and decoder for detection tasks but found that this design reduced performance on dense detection tasks, such

as nucleus detection. Therefore, we ultimately adopted a strategy that outputs bounding box coordinates directly in relative terms. These enhancements significantly improve the model’s performance on multi-scale feature extraction and fine-grained pathological visual tasks.

## 4.2. Prompt-Guided Detail Feature Completion

When using pathology LVLMs for WSI diagnostic analysis, only the thumbnail of the WSI can be used as input, resulting in substantial information loss that affects diagnostic accuracy. Our proposed PGDFC strategy dynamically completes missing information based on specific task requirements while maintaining inference efficiency, as shown in Figure 3. Specifically, we first remove elements corresponding to image background regions from  $\Psi_{(N+M),e_v}$  and select the top- $S$  elements with the highest values from the remaining elements, denoting their indices as  $\mathbf{I} = \{i_1, i_2, \dots, i_S\}$ . Then, using the index set  $\mathbf{I}$ , we locate the corresponding tile regions in the original WSI and extract high-resolution patches from these regions, denoted as  $\hat{x}_v = \{\hat{x}_v^1, \hat{x}_v^2, \dots, \hat{x}_v^S\}$ .

We use  $\mathcal{V}$  to extract features for each image in  $\hat{x}_v$ , obtaining a set of feature sequences  $\hat{e}_v = \{\hat{e}_v^1, \hat{e}_v^2, \dots, \hat{e}_v^S\}$ , where  $\hat{e}_v^s = \mathcal{V}(\hat{x}_v^s)$ . Simultaneously, we encode the positional information of each patch using textual descriptions, denoted as  $\hat{x}_t = \{\hat{x}_t^1, \hat{x}_t^2, \dots, \hat{x}_t^S\}$ , and obtain the corresponding text embeddings  $\hat{e}_t = \{\hat{e}_t^1, \hat{e}_t^2, \dots, \hat{e}_t^S\}$  through  $\mathcal{T}$ , where  $\hat{e}_t^s = \mathcal{T}(\hat{x}_t^s)$ . By feeding  $\hat{e}_v$  and  $\hat{e}_t$  along with the original inputs  $e_v$  and  $e_t$  into  $\mathcal{M}$ , we can obtain the final diagnostic result  $y = \mathcal{M}(e_v, e_t, \hat{e}_v, \hat{e}_t)$ . To mitigate the impact of the large number of  $\hat{e}_v$  tokens on  $\mathcal{M}$ ’s inference efficiency, we use the average pooling on each element of  $\hat{e}_v$  to reduce the token count of it.

## 5. Experiments

In this section, we first provide the implementation details of OmniPath, followed by comparative results across multiple tasks. Finally, we conduct ablation studies on the key components of OmniPath.

### 5.1. Implementation Details

Based on the pretrained LLaVA-1.5-13B [30], we constructed OmniPath by replacing its CLIP ViT-L 336px [35] visual encoder with SigLIP ViT-SO 384px [53] and integrating UNI [11] as an auxiliary vision encoder. The projector utilizes a two-layer MLP with GELU activation. The

Method	HCC-S	HCC-G	ICC-S	ICC-G	RCC-S	LUNG-S	LUNG-G	STAD-L	STAD-G	LNM	HCC-P	CRC-P
LLaVA-1.5	14.31	37.50	17.25	32.55	9.09	19.45	20.33	15.44	18.77	61.04	0.00	31.88
LLaVA-Med	15.32	35.42	23.56	38.53	10.39	23.88	26.48	18.59	19.95	63.21	8.45	32.78
Quilt-LLaVA	77.73	57.88	67.47	83.69	66.78	70.96	66.14	39.12	53.90	64.39	47.38	65.71
PA-LLaVA	77.96	53.05	70.84	74.45	73.75	74.74	70.44	43.77	55.25	55.70	52.63	69.64
OmniPath	<b>98.40</b>	<b>70.83</b>	<b>87.76</b>	<b>99.08</b>	<b>87.88</b>	<b>98.72</b>	<b>83.09</b>	<b>52.72</b>	<b>76.69</b>	<b>79.22</b>	<b>66.10</b>	<b>85.51</b>

Table 2. Performance comparison on slide-level pathology diagnostic tasks.

Metric	Cancer Region						Tissue Structure			Cell Nucleus		
	HCC	ICC	RCC	GBM	LUAD	BC	LD	VD	ND	MoNuSeg	NuCLS	PanNuke
F1-Score	92.13	100.00	90.91	40.85	90.91	41.38	82.70	89.52	72.50	83.98	34.30	45.30
IoU	91.97	91.85	89.59	73.85	87.96	72.75	87.34	83.00	79.75	79.65	44.98	59.99

Table 3. Performance of OmniPath in pathology referring detection tasks.

mask encoder is implemented with ResNet-50 [19], while the mask decoder follows SAM’s [24] decoder architecture but directly uses the LVLm’s vision encoder to replace SAM’s original image encoder for feature extraction. During training, all modules of OmniPath participate in end-to-end training with no parameter freezing. We created a multitask dataset encompassing 20 organs and approximately 490,000 samples for model training (see supplementary material for detailed data sources and construction methods). Unlike the two-stage training strategy commonly adopted by existing LVLms, OmniPath requires only a single-stage fine-tuning: trained for 2 epochs on 8 NVIDIA A800 GPUs using the AdamW optimizer, with a learning rate of  $2e-5$  and a global batch size of 128. We set  $S = 8$ , and compare OmniPath with LLaVA-1.5 [30], LLaVA-Med [27], Quilt-LLaVA [36], and PA-LLaVA [13].

## 5.2. Comparison on Pathology Diagnostic Tasks

To evaluate the pathology diagnostic performance of various LVLms, we conducted a series of clinically relevant pathology diagnostic experiments, divided by diagnostic granularity into patch-level and slide-level categories. The patch-level experiments included subtyping and grading tasks for a range of common cancers, such as hepatocellular carcinoma subtyping (HCC-S) and grading (HCC-G), intrahepatic cholangiocarcinoma subtyping (ICC-S) and grading (ICC-G), renal cell carcinoma subtyping (RCC-S), lung cancer subtyping (LUNG-S) and grading (LUNG-G), gastric adenocarcinoma Lauren subtyping (STAD-L) and grading (STAD-G). In addition, other tasks related to pathology concept recognition or diagnosis included: microvascular invasion identification (MVI), neural invasion identification (NI), pan-cancer identification across 32 types (PanCancer), organ classification (OC), tissue classification (TC), tumor-infiltrating lymphocyte identification (TIL), microsatellite instability detection in colorectal cancer (MSI), and seven-class gastric lesion recognition (GLR-7). The accuracy of each model on these tasks is detailed in Table 1.

Slide-level experiments included not only the same subtyping and grading tasks as the patch-level but also additional tasks, such as lymph node metastasis diagnosis (LNM), HCC prognosis prediction (HCC-P), and colorectal cancer prognosis prediction (CRC-P), using WSI thumbnails as image input. The accuracy of each model on slide-level tasks is presented in Table 2.

It can be observed that OmniPath achieves the best performance across all patch-level and slide-level pathological diagnosis tasks. For most cancer subtype classification and grading tasks, OmniPath achieves accuracy rates exceeding 70%, and in many cases, surpassing 90%. In contrast, the accuracy rates of other models are generally below 70%. This demonstrates that OmniPath is more suitable for clinical applications to assist pathologists in diagnosis. Furthermore, OmniPath also exhibits strong recognition capabilities for features such as microvascular invasion, neural invasion, and tumor-infiltrating lymphocytes. This significantly reduces the extensive effort required by pathologists to meticulously examine detailed pathological lesions during slide review.

## 5.3. Comparison on Zero-Shot Classification Tasks

To evaluate the clinical generalization capability of OmniPath, we employed a zero-shot classification paradigm, testing on several widely-used academic pathology datasets that were not included in the training set. The evaluation covered two levels: patch-level tasks using the CCRCC [6], MHIST [47], and NCT-CRC [32] datasets, and slide-level tasks using the PANDA [7], DHMC [48], and CAMELYON17 [29] datasets. Using a closed-ended question-answering approach, the model was required to classify images into predefined categories specific to each dataset. The performance comparison of all models on these zero-shot test sets is presented in Table 4.

It is shown that OmniPath consistently outperforms other models across both patch-level and slide-level datasets in zero-shot classification tasks, highlighting its strong gener-



Method	Patch-Level Dataset			Slide-Level Dataset		
	CCRCC	MHIST	NCT-CRC	PANDA	DHMC	CAMELYON17
LLaVA-1.5	15.47	69.31	11.58	62.43	31.84	19.44
LLaVA-Med	13.67	33.82	12.71	57.40	10.57	39.03
Quilt-LLaVA	17.18	68.46	13.84	64.06	28.48	48.27
PA-LLaVA	15.43	<b>70.02</b>	15.19	70.33	27.88	34.45
OmniPath	<b>23.67</b>	69.77	<b>20.67</b>	<b>79.15</b>	<b>34.62</b>	<b>59.33</b>

Table 4. Comparison on zero-shot classification tasks.

Metric	Cancer Region						Tissue Structure		
	HCC	ICC	RCC	GBM	LUAD	BC	NS	NIS	LNMS
IoU	91.65	88.25	80.03	39.34	87.08	64.16	81.31	54.01	50.96
Dice	95.51	93.60	85.11	50.01	93.03	74.64	89.23	62.14	56.94

Table 5. OmniPath’s performance in referring segmentation.

alization ability in pathological image analysis. Notably, on the PANDA and CAMELYON17 slide-level datasets, OmniPath achieved the highest accuracy rates of 79.15% and 59.33%, respectively, which significantly surpasses the performance of other models. This superior performance in zero-shot classification indicates OmniPath’s robustness in handling diverse pathological image data and reinforces its potential for clinical applications where labeled training data may be limited.

#### 5.4. Detection and Segmentation Performance

In pathological diagnosis, detection and segmentation tasks are as critical as classification tasks. For instance, assessing microvascular invasion requires counting cancer cell nuclei within blood vessels, which relies on accurate referring detection. Given that existing pathological LVLMS lack detection and segmentation capabilities, this part presents only OmniPath’s performance on these tasks. The detection tasks cover various cancer region identifications, including HCC, ICC, RCC, glioblastoma (GBM), lung adenocarcinoma (LUAD), and bladder cancer (BC). Additionally, it involves detecting tissue structures such as lymph nodes (LD), vessels (VD), and nerves (ND), as well as cell nuclei detection in datasets like MoNuSeg [25] (without categories), NuCLS [3], and PanNuke [18] (with categories). The segmentation tasks not only include the segmentation of cancer regions covered by the detection tasks but also nerve segmentation (NS), nerve invasion region segmentation (NIS), and lymph node metastasis segmentation (LNMS). Detection tasks are evaluated using F1-score and IoU, while segmentation tasks are assessed using the IoU and Dice coefficient. Table 3 and Table 5 show the detection and segmentation performance, respectively.

While OmniPath’s performance may not surpass specialized smaller models on certain tasks, it offers a unique advantage in inferential capabilities. As shown in Figure 1, OmniPath can accurately detect cancer cell nuclei within blood vessels according to instructions—an ability that current specialized small models find challenging to achieve.

Task	w/o PGDFC	Random	w/ PGDFC
HCC-S	20.14	79.46	<b>98.40</b>
HCC-G	52.84	45.83	<b>70.83</b>
ICC-S	85.71	85.71	<b>87.76</b>
ICC-G	66.37	83.72	<b>99.08</b>
RCC-S	60.61	75.76	<b>87.88</b>
LUNG-S	96.58	96.43	<b>98.72</b>
LUNG-G	65.54	63.21	<b>83.09</b>
STAD-L	44.60	35.07	<b>52.72</b>
STAD-G	72.92	75.31	<b>76.69</b>
Avg	62.81	71.17	<b>83.91</b>

Table 6. Ablation study of PGDFC strategy. “Random” refers to selecting  $\hat{x}_v$  at random, rather than selecting based on  $\mathbf{I}$ .

#### 5.5. Ablation Study

The ablation study in Table 6 underscores the effectiveness of the PGDFC strategy in enhancing OmniPath’s performance across WSI diagnostic tasks. Three configurations were tested: (1) without PGDFC, (2) replacing the top-S elements in  $\Psi_{(N+M),e_v}$  with random selection of  $\hat{x}_v$ , and (3) with the designed PGDFC strategy. Removing PGDFC resulted in an average accuracy drop of 21.1%, while random selection led to a decrease of 12.7% compared to using PGDFC. Notably, for tasks like HCC-S and ICC-G, PGDFC boosted accuracy significantly, demonstrating its ability to enhance model focus on essential features, which is critical for accurate diagnosis across complex pathology tasks. In certain tasks, such as HCC-G and STAD-L, random selection results in performance that is even lower than without PGDFC, indicating that incorrectly supplementing detailed features can also impair model performance.

#### 6. Conclusion

This paper presents OmniPath, a pathology-focused LVLMS shaped by two key strategies addressing limitations in existing models. The mixed task-guided feature enhancement strategy ensures precise lesion-specific feature extraction, while the prompt-guided detail feature completion strategy combines global context with fine-grained detail to meet clinical needs. Together, these approaches enable comprehensive and balanced feature extraction, validated across diverse pathology tasks, positioning OmniPath as a transformative tool in digital pathology.

**Limitations and Future Work.** OmniPath faces three main limitations: First, the model lacks sufficient depth in medical and pathological expertise due to training data primarily consisting of image-caption pairs, with limited integration of advanced pathology knowledge and literature. To address this, we plan to enhance the model’s knowledge base using RAG techniques. Second, its performance in zero-shot classification tasks remains suboptimal. We will introduce a multi-agent framework to enable specialized agents to assist with more accurate diagnoses in complex cases. Finally, the model’s reasoning capability is not



yet sufficient for independent diagnosis. To resolve this, we will collect pathologists’ diagnostic process data and integrate it with larger-scale LLMs, aiming to enhance reasoning and achieve autonomous diagnosis, ultimately reducing physicians’ workload.

## References

- [1] Josh Achiam, Steven Adler, Sandhini Agarwal, Lama Ahmad, Ilge Akkaya, Florencia Leoni Aleman, Diogo Almeida, Janko Altenschmidt, Sam Altman, Shyamal Anadkat, et al. Gpt-4 technical report. *arXiv preprint arXiv:2303.08774*, 2023. 1, 3
- [2] Faruk Ahmed, Andrew SELLERGRÉN, Lin Yang, Shawn Xu, Boris Babenko, Abbi Ward, Niels Olson, Arash Mohtashamian, Yossi Matias, Greg S Corrado, et al. Pathalign: A vision-language model for whole slide images in histopathology. *arXiv preprint arXiv:2406.19578*, 2024. 1, 3
- [3] Mohamed Amgad, Lamees A Atteya, Hagar Hussein, Kareem Hosny Mohammed, Ehab Hafiz, Maha AT Elsebaie, Ahmed M Alhusseiny, Mohamed Atef AlMoslemany, Abdelmagid M Elmatboly, Philip A Pappalardo, et al. Nucleus: A scalable crowdsourcing approach and dataset for nucleus classification and segmentation in breast cancer. *Giga-Science*, 11:giac037, 2022. 8
- [4] Jinze Bai, Shuai Bai, Shusheng Yang, Shijie Wang, Sinan Tan, Peng Wang, Junyang Lin, Chang Zhou, and Jingren Zhou. Qwen-vl: A versatile vision-language model for understanding, localization, text reading, and beyond. *arXiv preprint arXiv:2308.12966*, 1(2):3, 2023. 1
- [5] Tom B Brown. Language models are few-shot learners. *arXiv preprint arXiv:2005.14165*, 2020. 1
- [6] Otso Brummer, Petri Pölönen, Satu Mustjoki, and Oscar Brück. Integrative analysis of histological textures and lymphocyte infiltration in renal cell carcinoma using deep learning. *bioRxiv*, pages 2022–08, 2022. 7
- [7] Wouter Bulten, Kimmo Kartasalo, Po-Hsuan Cameron Chen, Peter Ström, Hans Pinckaers, Kunal Nagpal, Yuannan Cai, David F Steiner, Hester Van Boven, Robert Vink, et al. Artificial intelligence for diagnosis and gleason grading of prostate cancer: the panda challenge. *Nature medicine*, 28(1):154–163, 2022. 7
- [8] Keqin Chen, Zhao Zhang, Weili Zeng, Richong Zhang, Feng Zhu, and Rui Zhao. Shikra: Unleashing multimodal llm’s referential dialogue magic. *arXiv preprint arXiv:2306.15195*, 2023. 1
- [9] Pingyi Chen, Chenglu Zhu, Sunyi Zheng, Honglin Li, and Lin Yang. Wsi-vqa: Interpreting whole slide images by generative visual question answering. In *European Conference on Computer Vision*, pages 401–417. Springer, 2025. 2
- [10] Richard J Chen, Chengkuan Chen, Yicong Li, Tiffany Y Chen, Andrew D Trister, Rahul G Krishnan, and Faisal Mahmood. Scaling vision transformers to gigapixel images via hierarchical self-supervised learning. In *Proceedings of the IEEE/CVF Conference on Computer Vision and Pattern Recognition*, pages 16144–16155, 2022. 1, 3
- [11] Richard J Chen, Tong Ding, Ming Y Lu, Drew FK Williamson, Guillaume Jaume, Andrew H Song, Bowen Chen, Andrew Zhang, Daniel Shao, Muhammad Shaban, et al. Towards a general-purpose foundation model for computational pathology. *Nature Medicine*, 30(3):850–862, 2024. 1, 3, 6
- [12] Yangyi Chen, Xingyao Wang, Hao Peng, and Heng Ji. A single transformer for scalable vision-language modeling. *arXiv preprint arXiv:2407.06438*, 2024. 1
- [13] Dawei Dai, Yuanhui Zhang, Long Xu, Qianlan Yang, Xiaojing Shen, Shuyin Xia, and Guoyin Wang. Pa-llava: A large language-vision assistant for human pathology image understanding. *arXiv preprint arXiv:2408.09530*, 2024. 1, 3, 5, 7
- [14] Abhimanyu Dubey, Abhinav Jauhri, Abhinav Pandey, Abhishek Kadian, Ahmad Al-Dahle, Aiesha Letman, Akhil Mathur, Alan Schelten, Amy Yang, Angela Fan, et al. The llama 3 herd of models. *arXiv preprint arXiv:2407.21783*, 2024. 1
- [15] Zunlei Feng, Zhonghua Wang, Xinchao Wang, Yining Mao, Thomas Li, Jie Lei, Yuexuan Wang, and Mingli Song. Mutual-complementing framework for nuclei detection and segmentation in pathology image. In *Proceedings of the IEEE/CVF International Conference on Computer Vision*, pages 4036–4045, 2021. 1, 3
- [16] Zunlei Feng, Zhonghua Wang, Xinchao Wang, Xiuming Zhang, Lechao Cheng, Jie Lei, Yuexuan Wang, and Mingli Song. Edge-competing pathological liver vessel segmentation with limited labels. In *Proceedings of the AAAI Conference on Artificial Intelligence*, pages 1325–1333, 2021. 1, 3
- [17] Jevgenij Gamper and Nasir Rajpoot. Multiple instance captioning: Learning representations from histopathology text-books and articles. In *Proceedings of the IEEE/CVF conference on computer vision and pattern recognition*, pages 16549–16559, 2021. 2
- [18] Jevgenij Gamper, Navid Alemi Koohbanani, Ksenija Benes, Simon Graham, Mostafa Jahanifar, Syed Ali Khurram, Ayesha Azam, Katherine Hewitt, and Nasir Rajpoot. Pan-nuke dataset extension, insights and baselines. *arXiv preprint arXiv:2003.10778*, 2020. 8
- [19] Kaiming He, Xiangyu Zhang, Shaoqing Ren, and Jian Sun. Deep residual learning for image recognition. In *Proceedings of the IEEE conference on computer vision and pattern recognition*, pages 770–778, 2016. 7
- [20] Xuehai He, Yichen Zhang, Luntian Mou, Eric Xing, and Pengtao Xie. Pathvqa: 30000+ questions for medical visual question answering. *arXiv preprint arXiv:2003.10286*, 2020. 2
- [21] Zhi Huang, Federico Bianchi, Mert Yuksekogun, Thomas J Montine, and James Zou. A visual-language foundation model for pathology image analysis using medical twitter. *Nature medicine*, 29(9):2307–2316, 2023. 2
- [22] Wisdom Ikezogwo, Saygin Seyfioglu, Fatemeh Ghezloo, Dylan Geva, Fatwir Sheikh Mohammed, Pavan Kumar Anand, Ranjay Krishna, and Linda Shapiro. Quilt-1m: One million image-text pairs for histopathology. *Advances in neural information processing systems*, 36, 2024. 2

- [23] Maximilian Ilse, Jakub Tomczak, and Max Welling. Attention-based deep multiple instance learning. In *International conference on machine learning*, pages 2127–2136. PMLR, 2018. 3
- [24] Alexander Kirillov, Eric Mintun, Nikhila Ravi, Hanzi Mao, Chloe Rolland, Laura Gustafson, Tete Xiao, Spencer Whitehead, Alexander C Berg, Wan-Yen Lo, et al. Segment anything. In *Proceedings of the IEEE/CVF International Conference on Computer Vision*, pages 4015–4026, 2023. 7
- [25] Neeraj Kumar, Ruchika Verma, Deepak Anand, Yanning Zhou, Omer Fahri Onder, Efstratios Tsougenis, Hao Chen, Pheng-Ann Heng, Jiahui Li, Zhiqiang Hu, et al. A multi-organ nucleus segmentation challenge. *IEEE transactions on medical imaging*, 39(5):1380–1391, 2019. 8
- [26] Xin Lai, Zhuotao Tian, Yukang Chen, Yanwei Li, Yuhui Yuan, Shu Liu, and Jiaya Jia. Lisa: Reasoning segmentation via large language model. In *Proceedings of the IEEE/CVF Conference on Computer Vision and Pattern Recognition*, pages 9579–9589, 2024. 1
- [27] Chunyuan Li, Cliff Wong, Sheng Zhang, Naoto Usuyama, Haotian Liu, Jianwei Yang, Tristan Naumann, Hoifung Poon, and Jianfeng Gao. Llava-med: Training a large language-and-vision assistant for biomedicine in one day. In *Advances in Neural Information Processing Systems*, pages 28541–28564. Curran Associates, Inc., 2023. 4, 7
- [28] Junnan Li, Dongxu Li, Silvio Savarese, and Steven Hoi. Blip-2: Bootstrapping language-image pre-training with frozen image encoders and large language models. In *International conference on machine learning*, pages 19730–19742. PMLR, 2023. 3
- [29] Geert Litjens, Peter Bandi, Babak Ehteshami Bejnordi, Oscar Geessink, Maschenka Balkenhol, Peter Bult, Altuna Halilovic, Meyke Hermesen, Rob Van de Loo, Rob Vogels, et al. 1399 h&e-stained sentinel lymph node sections of breast cancer patients: the camelyon dataset. *GigaScience*, 7(6):giy065, 2018. 7
- [30] Haotian Liu, Chunyuan Li, Qingyang Wu, and Yong Jae Lee. Visual instruction tuning. *Advances in neural information processing systems*, 36, 2024. 1, 3, 6, 7
- [31] Ming Y Lu, Bowen Chen, Drew FK Williamson, Richard J Chen, Melissa Zhao, Aaron K Chow, Kenji Ikemura, Ahrong Kim, Dimitra Pouli, Ankush Patel, et al. A multimodal generative ai copilot for human pathology. *Nature*, pages 1–3, 2024. 1, 3, 5
- [32] Marc Macenko, Marc Niethammer, J. S. Marron, David Borland, John T. Woosley, Xiaojun Guan, Charles Schmitt, and Nancy E. Thomas. A method for normalizing histology slides for quantitative analysis. In *2009 IEEE International Symposium on Biomedical Imaging: From Nano to Macro*, pages 1107–1110, 2009. 7
- [33] Maxime Oquab, Timothée Darcet, Théo Moutakanni, Huy Vo, Marc Szafraniec, Vasil Khalidov, Pierre Fernandez, Daniel Haziza, Francisco Massa, Alaaeldin El-Nouby, et al. Dinov2: Learning robust visual features without supervision. *arXiv preprint arXiv:2304.07193*, 2023. 6
- [34] Long Ouyang, Jeffrey Wu, Xu Jiang, Diogo Almeida, Carroll Wainwright, Pamela Mishkin, Chong Zhang, Sandhini Agarwal, Katarina Slama, Alex Ray, et al. Training language models to follow instructions with human feedback. *Advances in neural information processing systems*, 35:27730–27744, 2022. 1, 3
- [35] Alec Radford, Jong Wook Kim, Chris Hallacy, Aditya Ramesh, Gabriel Goh, Sandhini Agarwal, Girish Sastry, Amanda Askell, Pamela Mishkin, Jack Clark, et al. Learning transferable visual models from natural language supervision. In *International conference on machine learning*, pages 8748–8763. PMLR, 2021. 3, 5, 6
- [36] Mehmet Saygin Seyfioglu, Wisdom O Ikezogwo, Fatemeh Ghezloo, Ranjay Krishna, and Linda Shapiro. Quilt-llava: Visual instruction tuning by extracting localized narratives from open-source histopathology videos. In *Proceedings of the IEEE/CVF Conference on Computer Vision and Pattern Recognition*, pages 13183–13192, 2024. 1, 2, 3, 4, 5, 7
- [37] George Shaikovski, Adam Casson, Kristen Severson, Eric Zimmermann, Yi Kan Wang, Jeremy D Kunz, Juan A Retamero, Gerard Oakley, David Klimstra, Christopher Kanan, et al. Prism: A multi-modal generative foundation model for slide-level histopathology. *arXiv preprint arXiv:2405.10254*, 2024. 1, 3
- [38] Zhuchen Shao, Hao Bian, Yang Chen, Yifeng Wang, Jian Zhang, Xiangyang Ji, et al. Transmil: Transformer based correlated multiple instance learning for whole slide image classification. *Advances in neural information processing systems*, 34:2136–2147, 2021. 3
- [39] Yuxuan Sun, Yunlong Zhang, Yixuan Si, Chenglu Zhu, Zhongyi Shui, Kai Zhang, Jingxiong Li, Xingheng Lyu, Tao Lin, and Lin Yang. Pathgen-1.6 m: 1.6 million pathology image-text pairs generation through multi-agent collaboration. *arXiv preprint arXiv:2407.00203*, 2024. 1, 2, 3
- [40] Yuxuan Sun, Chenglu Zhu, Sunyi Zheng, Kai Zhang, Lin Sun, Zhongyi Shui, Yunlong Zhang, Honglin Li, and Lin Yang. Pathasst: A generative foundation ai assistant towards artificial general intelligence of pathology. In *Proceedings of the AAAI Conference on Artificial Intelligence*, pages 5034–5042, 2024. 2, 3, 5
- [41] Yuxuan Sun, Hao Wu, Chenglu Zhu, Sunyi Zheng, Qizi Chen, Kai Zhang, Yunlong Zhang, Dan Wan, Xiaoxiao Lan, Mengyue Zheng, et al. Pathmmu: A massive multimodal expert-level benchmark for understanding and reasoning in pathology. In *European Conference on Computer Vision*, pages 56–73. Springer, 2025. 1, 2, 3
- [42] Kevin Thandiackal, Boqi Chen, Pushpak Pati, Guillaume Jaume, Drew FK Williamson, Maria Gabrani, and Orcun Goksel. Differentiable zooming for multiple instance learning on whole-slide images. In *European Conference on Computer Vision*, pages 699–715. Springer, 2022. 3
- [43] Hugo Touvron, Thibaut Lavril, Gautier Izacard, Xavier Martinet, Marie-Anne Lachaux, Timothée Lacroix, Baptiste Rozière, Naman Goyal, Eric Hambro, Faisal Azhar, et al. Llama: Open and efficient foundation language models. *arXiv preprint arXiv:2302.13971*, 2023. 1
- [44] Hugo Touvron, Louis Martin, Kevin Stone, Peter Albert, Amjad Almahairi, Yasmine Babaei, Nikolay Bashlykov, Soumya Batra, Prajjwal Bhargava, Shrutu Bhosale, et al.

- Llama 2: Open foundation and fine-tuned chat models. *arXiv preprint arXiv:2307.09288*, 2023. 1
- [45] Eugene Vorontsov, Alican Bozkurt, Adam Casson, George Shaikovski, Michal Zelechowski, Kristen Severson, Eric Zimmermann, James Hall, Neil Tenenholtz, Nicolo Fusi, et al. A foundation model for clinical-grade computational pathology and rare cancers detection. *Nature medicine*, pages 1–12, 2024. 1, 3
  - [46] Xiyue Wang, Junhan Zhao, Eliana Marostica, Wei Yuan, Jietian Jin, Jiayu Zhang, Ruijiang Li, Hongping Tang, Kanran Wang, Yu Li, et al. A pathology foundation model for cancer diagnosis and prognosis prediction. *Nature*, pages 1–9, 2024. 1, 3
  - [47] Jerry Wei, Arief Suriawinata, Bing Ren, Xiaoying Liu, Mikhail Lisovsky, Louis Vaickus, Charles Brown, Michael Baker, Naofumi Tomita, Lorenzo Torresani, et al. A petri dish for histopathology image analysis. In *Artificial Intelligence in Medicine: 19th International Conference on Artificial Intelligence in Medicine, AIME 2021, Virtual Event, June 15–18, 2021, Proceedings*, pages 11–24. Springer, 2021. 7
  - [48] Jason W Wei, Laura J Tafe, Yevgeniy A Linnik, Louis J Vaickus, Naofumi Tomita, and Saeed Hassanpour. Pathologist-level classification of histologic patterns on resected lung adenocarcinoma slides with deep neural networks. *Scientific reports*, 9(1):3358, 2019. 7
  - [49] Xiaomin Wu, Rui Xu, Pengchen Wei, Wenkang Qin, Peixiang Huang, Ziheng Li, and Lin Luo. Pathinsight: Instruction tuning of multimodal datasets and models for intelligence assisted diagnosis in histopathology. *arXiv preprint arXiv:2408.07037*, 2024. 1, 3
  - [50] Gang Xu, Zhigang Song, Zhuo Sun, Calvin Ku, Zhe Yang, Cancheng Liu, Shuhao Wang, Jianpeng Ma, and Wei Xu. Camel: A weakly supervised learning framework for histopathology image segmentation. In *Proceedings of the IEEE/CVF International Conference on computer vision*, pages 10682–10691, 2019. 3
  - [51] Hanwen Xu, Naoto Usuyama, Jaspreet Bagga, Sheng Zhang, Rajesh Rao, Tristan Naumann, Cliff Wong, Zelalem Gero, Javier González, Yu Gu, et al. A whole-slide foundation model for digital pathology from real-world data. *Nature*, pages 1–8, 2024. 1, 3
  - [52] Xiaotian Yu, Zunlei Feng, Mingli Song, Yuexuan Wang, Xiuming Zhang<sup>13</sup>, and Thomas Li. Tendentious noise-rectifying framework for pathological hcc grading. In *British Machine Vision Conference*, 2021. 1, 3
  - [53] Xiaohua Zhai, Basil Mustafa, Alexander Kolesnikov, and Lucas Beyer. Sigmoid loss for language image pre-training. In *Proceedings of the IEEE/CVF International Conference on Computer Vision*, pages 11975–11986, 2023. 6
  - [54] Shengxuming Zhang, Tianqi Shi, Yang Jiang, Xiuming Zhang, Jie Lei, Zunlei Feng, and Mingli Song. A loopback network for explainable microvascular invasion classification. In *Proceedings of the IEEE/CVF Conference on Computer Vision and Pattern Recognition (CVPR)*, pages 7443–7453, 2023. 1, 3, 5